

A methodology to investigate and optimise the crashworthiness response of foam-filled twelve right angles thin-walled structures under axial impact

Liang, R., Liu, X., Hu, Y., Jiang, C. & Bastien, C

Author post-print (accepted) deposited by Coventry University's Repository

Original citation & hyperlink:

Liang, R, Liu, X, Hu, Y, Jiang, C & Bastien, C 2023, 'A methodology to investigate and optimise the crashworthiness response of foam-filled twelve right angles thin-walled structures under axial impact', *Composite Structures*, vol. 310, 116736.

<https://doi.org/10.1016/j.compstruct.2023.116736>

DOI 10.1016/j.compstruct.2023.116736

ISSN 0263-8223

ESSN 1879-1085

Publisher: Elsevier

© 2023, Elsevier. Licensed under the Creative Commons Attribution-NonCommercial-NoDerivatives 4.0 International

<http://creativecommons.org/licenses/by-nc-nd/4.0/>

Copyright © and Moral Rights are retained by the author(s) and/ or other copyright owners. A copy can be downloaded for personal non-commercial research or study, without prior permission or charge. This item cannot be reproduced or quoted extensively from without first obtaining permission in writing from the copyright holder(s). The content must not be changed in any way or sold commercially in any format or medium without the formal permission of the copyright holders.

This document is the author's post-print version, incorporating any revisions agreed during the peer-review process. Some differences between the published version and this version may remain and you are advised to consult the published version if you wish to cite from it.

A methodology to investigate and optimise the crashworthiness response of foam-filled twelve right angles thin-walled structures under axial impact

Rui Liang^{1*}, Xi Liu^{2,*}, Yuanzhi Hu², Chengyue Jiang², Christophe Bastien³

1. School of Automobile Engineering, Guilin University of Aerospace Technology, Guilin 541004, China;
2. Key Laboratory of Advanced Manufacture Technology for Automobile Parts, Ministry of Education, Chongqing University of Technology, Chongqing 400054, China;
3. Institute for Future Transport and Cities, Coventry University, Coventry CV1 2TE, UK

Abstract: Multi-cell and foam-filled structures have shown outstanding crashworthiness capacities. As a result, foam-filled twelve right angles thin-walled structures (FTRATS), an integrator of them, can be excellent energy absorber candidates in the vehicle body structure. This paper presents a new methodology to investigate the crashworthiness potential of a series of novel FTRATS with different topological distributions. The base computer FTRATS model was correlated using existing experiments based on a single core thin-walled square tube filled with foam, then followed by a dynamic response evaluation of 32 FTRATS configurations, with the purpose of finding the lowest peak crushing force (PCF), the highest specific energy absorption (SEA) and crash load efficiency (CLE). As the results were initially inconclusive, a complex proportional assessment (COPRAS) method was used to extract the configuration with the highest potential, suggesting that the five-cell FTRATS filled with foam at its periphery showed superior crashworthiness properties. This selection was followed by an optimization using adaptive multi-population genetic algorithm methods based on response surfaces methodology, kriging model and Optimal Latin hypercube design. The solution obtained generated a stable collapse, increased the CLE (63.94 %), lowered PCF (38.83%) and increased SEA (38.86%). This new and innovative process has shown that coupling COPRAS and optimisation lead to an unbiased and efficient method to study and optimize FTRATS structures.

Keywords: Foam-filled; Twelve right angles thin-walled structure; FTRATS; Crashworthiness; Energy absorption; Topology

*Co-first author

Corresponding Author: Email: liuxi@cqut.edu.cn (Xi Liu)

1. Introduction

Thin-walled structures have been widely utilized as energy absorbers in vehicle bumpers and other parts to protect passengers from severe injury [1], consequently, they naturally received substantial attention. A series of essential mathematical models and strength formulations have been proposed to investigate the crashworthiness capacities of rectangular, square, circular, and elliptic cross-section tubes [2-7]. These thin-walled structures exhibited outstanding energy absorption performance; however, they may not make the best use of material due to their relative simplicity.

The energy absorption significantly depends on the tube geometries [8]. As an increasing number of corners of the cross-section can significantly increase thin-walled structures' crush strength [9], numerous studies have tried to improve the thin-walled structure's energy absorption properties by proposing various cross-section tubes. For instance, star-shaped [8], triangular [10, 11], hexagonal [12-15], octagonal [16, 17], and twelve right angles [18, 19] structures have been studied using finite element, mathematical and experimental methods. All the structures mentioned above show various numbers of corners and angles, however, thin-walled structures can present more effective energy absorption capacities when their corner angle is between 90° - 120° , and their number of corners is greater than eleven [20, 21]. Therefore, the twelve right angles tube with twelve 90° corners was reported as one of the most efficient energy absorbers [22-24].

Over the years, multi-cell thin-walled structures, the special thin-walled tube with multiple cells, have drawn increasing attention due to their excellent energy absorption and lightweight capacities [25-27]. For instance, Fang et al. [28], Zhang et al. [29] and Li et al. [30] illustrated a series of square tubes with numerous cells inside. Kim conducted square tubes with multi-cells in the corner part [31], while Tran proposed wall-to-wall and angle-to-wall multi-cell tubes [32]. Albak established a group of circumferentially corrugated square tubes with various sections added to its inner walls' edge junctions [33] and Ha et al. [34] and Gao et al. [35] proposed various hierarchical multi-cell structures.

To further improve the multi-cell structure's energy absorption and lightweight capacity, the aluminum foam has recently been employed as a filler in hollow multi-cell tubes [36-40]. Substantial essential experimental and numerical methods have been conducted [40-42]. Energy absorption characteristics, deformation and failure modes of foam-filled rectangular and cylindrical thin-walled structures subjected to compression and bending impact have been laid bare by numerous researchers [43-49]. Besides, foam-filled multi-cell tubes present a more stable deformation mode, resulting in superior crashworthiness performance [10, 42, 50, 51]. In addition, the cross-sectional configuration of multi-cell structures and distribution of foam filler can have a distinctive effect on energy absorption [52]. As a result, foam-filled twelve right angles thin-walled structures (FTRATS) with crashworthiness topology optimization may present excellent energy absorption and lightweight potential.

Nevertheless, while there has been much research on differently shaped foam-filled multi-cell tubes, to our knowledge, few studies have considered the energy absorption characteristics of FTRATS. This paper will therefore research the dynamic response and energy absorption properties of FTRATSs with various cross-section shapes and foam filler distributions under axial impact. The work will include a discrete multiobjective optimization approach based on optimal Latin hypercube design (Opt LHD) to optimize the FTRATSs' topological configuration to minimize peak crushing force (PCF) and maximize the specific energy absorption (SEA). The paper will propose an optimal FTRATS with improved crashworthiness beyond the best configuration chosen using the complicated proportional assessment (COPRAS).

2. Crashworthiness criteria

Specific energy absorption (SEA), peak crushing force (PCF), mean crushing force (MCF) and crash load efficiency (CLE) are the most frequently used crashworthiness indicators to study the collapse behavior of the energy absorbers of thin-walled structures [53-56].

In this paper, the energy absorption (EA) is determined as follows:

$$EA(d) = \int_0^d F(x)dx \quad (1)$$

where d is the deformation distance, F is the impact force, and x is the displacement.

The SEA can be denoted as:

$$SEA(d) = \frac{EA(d)}{M} \quad (2)$$

where M is the total mass of the specimen.

The MCF can be defined as:

$$MCF(d) = \frac{EA(d)}{d} \quad (3)$$

The CLE can be defined as:

$$CLE = \frac{MCF}{PCF} \quad (4)$$

The crashworthiness indicators of EA and MCF were calculated at the maximum compressed displacement herein.

3 Finite element modeling for FTRATS

3.1 Material properties definition

3.1.1 Aluminium foam

The aluminum foam manufactured by Hydro Aluminium a.s was employed as the foam core herein. The Deshpande Fleck foam material model MAT 154 was adopted to simulate the aluminum foam material [36, 41]. The yield criterion of the aluminum foam is defined as:

$$\Phi = \sigma_e - Y \quad (5)$$

Where Φ is the yield surface, Y the yield strength and σ_e the equivalent stress.

The σ_e is defined as:

$$\sigma_e^2 = \frac{1}{1 + \left(\frac{\alpha}{3}\right)^2} (\sigma_v^2 + \alpha^2 \sigma_m) \quad (6)$$

Where σ_v and σ_m denote the Von Mises effective stress and the mean stress, respectively. The α is a parameter that denotes the shape of the yield surface. The α is defined as:

$$\alpha^2 = \frac{9(1-2\nu^p)}{2(1+\nu^p)} \quad (7)$$

Where ν^p which is 0 in the plastic coefficient of contraction in an aluminum foam .

The strain hardening rule in this aluminum foam model was adopted as:

$$Y = \sigma_p + \gamma \frac{\varepsilon_e}{\varepsilon_D} + \alpha_2 \ln \left[\frac{1}{1 - (\varepsilon_e/\varepsilon_D)^\beta} \right] \quad (8)$$

Where ε_e is the equivalent strain. σ_p , γ , ε_D , α_2 , β are the material parameters that can be defined as:

$$\begin{cases} \left(\sigma_p, \alpha_2, \gamma, \frac{1}{\beta}, E_p \right) = C_0 + C_1 \left(\frac{\rho_f}{\rho_{f0}} \right)^q \\ \varepsilon_D = -\frac{9+\alpha^2}{3\alpha^2} \ln \left[\frac{\rho_f}{\rho_{f0}} \right] \end{cases} \quad (9)$$

Where the C_0 , C_1 , q are the constants shown in Table 1. ρ_f is the foam density, ρ_{f0} the base material density and E_p the foam Young's modulus of foam found at 2.3% permanent engineering strain.

Table 1. The material constants for aluminum foam [30,31]

	σ_p (MPa)	α_2 (MPa)	$1/\beta$	γ (MPa)	E_p (MPa)
C_0	0	0	0.22	0	0
C_1	720	140	320	42	0.33×10^6
q	2.33	0.45	4.66	1.42	2.45

3.1.2 Aluminium extrusions

The material of the thin-walled column used in this paper was an AA6060 T4 aluminum alloy, whose mechanical properties and the stress-strain relationship are given in Table 2 and Table 3, respectively. The material was modeled using a MAT24 LS-Dyna piecewise linear plasticity material model. As aluminum is not sensitive to strain rate [52], the rate-dependent effects, as well as material failure of the extruded geometry were not considered [1].

Table 2. The mechanical properties of the AA6060 T4 [36, 41]

Density	Young's modulus	Initial yield stress	Ultimate stress	Poisson's ratio	Power law exponent
$2.7 \times 10^3 \text{ kg/m}^3$	68.2 GPa	80 MPa	173 MPa	0.3	0.23

Table 3. Strain hardening data for AA6060 T4 [36, 41]

Plastic strain (%)	Plastic stress (MPa)
0.0	80
2.4	115
4.9	139
7.4	150
9.9	158
12.4	167
14.9	171

3.2 Finite element modeling

3.2.1 Geometry description and manufacturing process of the FTRATS

In order to comprehensively explore the effects of cross-sectional configurations and distribution of foam core filler on the crashworthiness of FTRATS, the full combinations of four twelve right angles thin-walled tubes and eight various distribution patterns of foam filler were initially investigated, as shown in Fig. 1 and Table 3. The research considered the four twelve right angles thin-walled tubes made of aluminum alloy AA 6060 T4 (outer sizes: 80 mm × 80 mm × 295 mm) and open-cell foam specimens. Note that the thickness of aluminum extrusions was adjusted to make all four aluminum extrusions with different geometries of the same mass, as shown in Fig.1.

In order to facilitate the comparison, the label A-B was applied to denote each topological configuration of FTRATS. 'A' represents the cross-section configurations, i.e., single cell tube (A1), triple cells tube (A3), five cells tube (A5) and seven cells tube (A7) and 'B' denotes one of the eight various distribution patterns of foam filler, i.e., foam-0, foam-1, foam-2, foam-3, foam-12, foam-13, foam-23, foam-123, as shown in Table 3. For instance, A5-3 represents a five-cell tube with a foam filler distribution foam-3. Besides, the tubular structure proposed in this paper can be manufactured by the laser welding process of the plate structure, which has little influence on the performance of the specimen when studying the dynamic significant deformation crashworthiness situation [57]. As a result, the weld seam was modeled as a coincident node connection. Further, the aluminum foam was machined into bars in order to obtain an exact fit into the extrusions [39]. Note that there is no bond between the multi-cell tube and the foam filler.

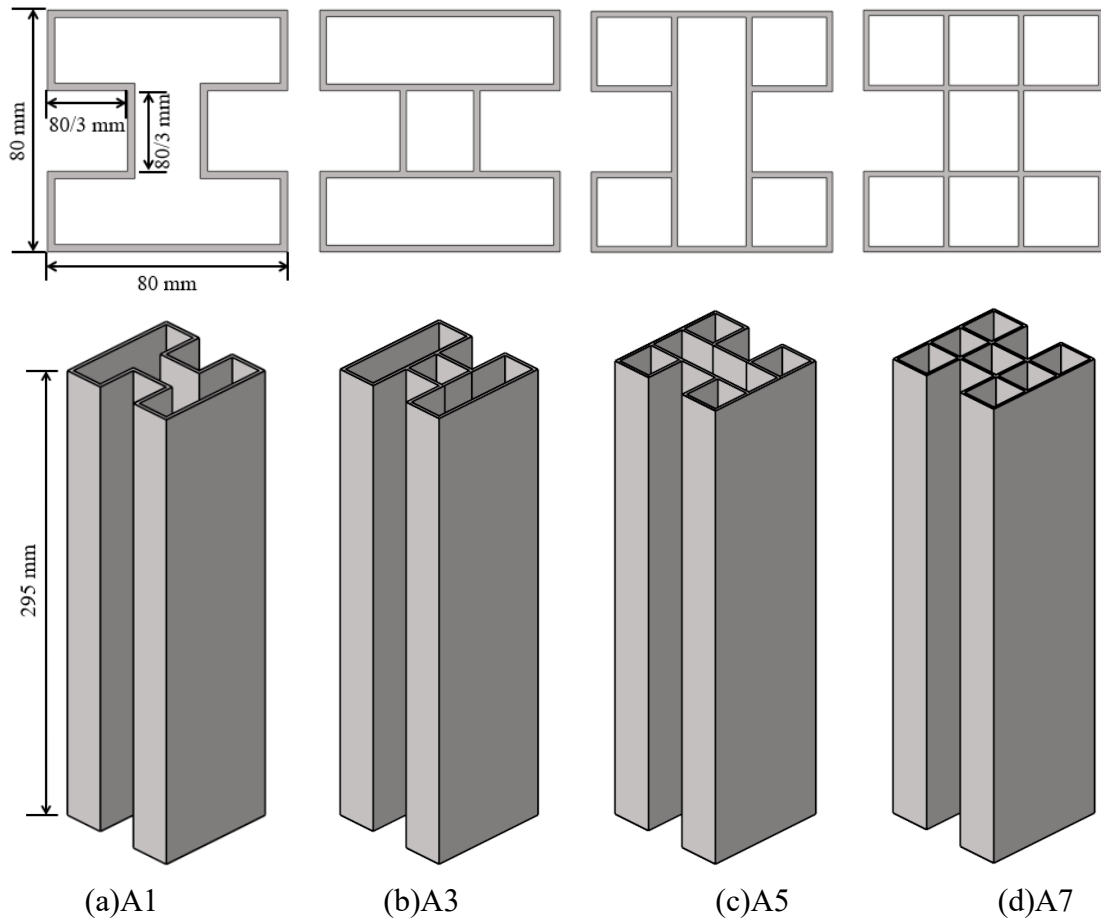
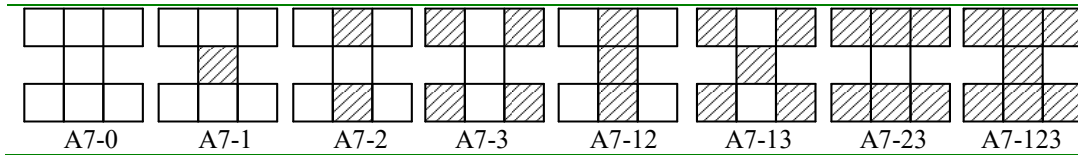


Fig.1. The topological configurations of aluminum extrusion (a) single cell tube, marked as A1, thickness $T_{A1}=2.45\text{mm}$; (b) triple cells tube, marked as A3, thickness $T_{A3}=2.177\text{mm}$; (c) five cells tube, marked as A5, thickness $T_{A5}=1.959\text{mm}$; (d) seven cells tube, marked as A7, thickness $T_{A7}=1.781\text{mm}$.

Table 3. FTRATSS topological configurations.

Single-cell tube							
A1-0	A1-1	A1-2	A1-3	A1-12	A1-13	A1-23	A1-123
Triple-cell tube							
A3-0	A3-1	A3-2	A3-3	A3-12	A3-13	A3-23	A3-123
Five-cell tube							
A5-0	A5-1	A5-2	A5-3	A5-12	A5-13	A5-23	A5-123
Seven-cell tube							



3.2.2 Dynamic experiment

This study uses the experimental setup from Langseth and Hopperstad [58] to calibrate the base finite element model. The test is illustrated in Fig 2. in which the FTRATS specimens are clamped at the lower end and free at the top and impacted with a projectile. A high-strength aluminum cover was placed at the top of the specimens to ensure a central impact. The specimens' force-displacement responses were calculated after filtering out the elastic vibrations set up in the projectile and cover during impact.

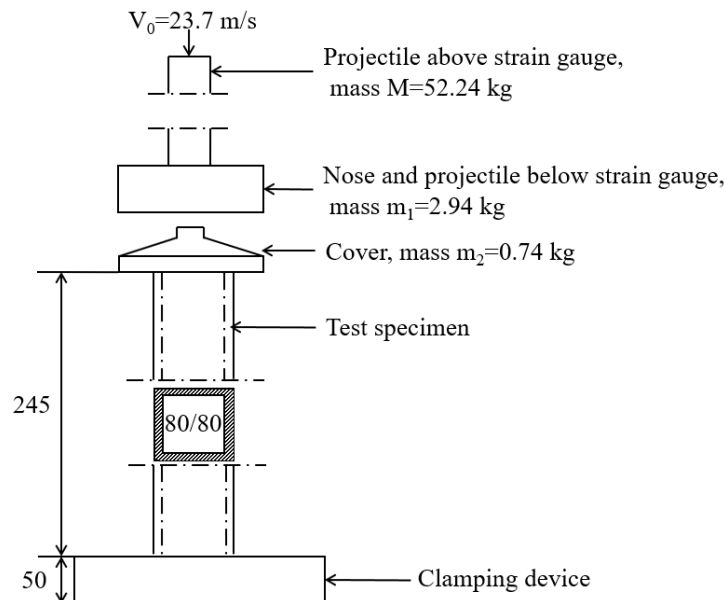


Fig.2 Test program and experimental details

3.2.3 Finite element model

A nonlinear finite element code LS-Dyna was utilized to create finite element (FE) models. The Belytschko-Lin-Tsay thin shell elements were employed to model the impactor, the tube wall and the clamping device, while the eight-node solid elements were adopted to simulate the aluminum foam core [36, 59]. The impactor and the clamping device were modeled as rigid. The "Automatic surface to surface" contact was applied to model the interface between the foam and structure walls, while the "Automatic single surface" contact was used for the structure wall and the foam core. Those contacts' static and dynamic coefficients of friction were set as 0.1, respectively. Fig. 3 shows the schematic of FTRATS' FE model. The impactor's equivalent mass was

56 kg, with an initial velocity of 23.7 m/s. The tube and foam core element sizes were adjusted as $2 \times 2 \text{ mm}^2$ and $4 \times 4 \text{ mm}^3$ to balance the accuracy of the numerical results and the computational cost.

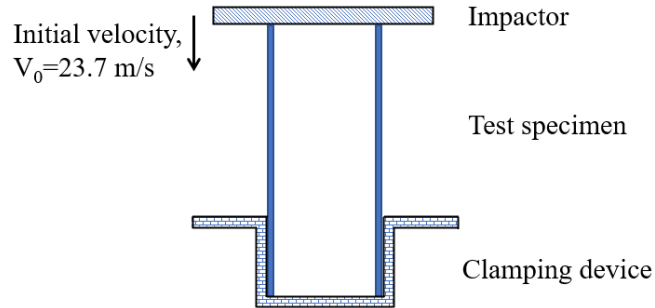
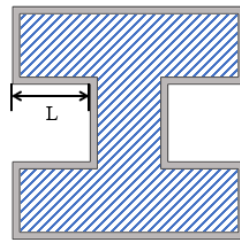


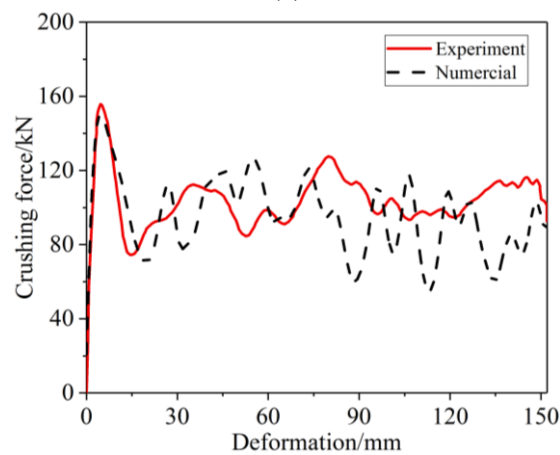
Fig.3. Schematic of FTRATS.

3.3 Validation of the finite element modeling

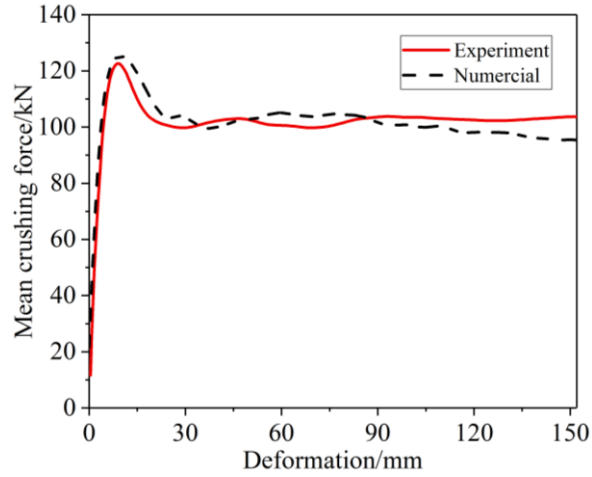
Hanssen et al. proposed many experiments to study the crashworthiness of single-cell AA6060 T4 aluminum foam-filled structure [39]. One of the geometries tested by Hanssen et al. is a single square cell filled with foam ($L=0$). This test, illustrated in Fig.4 (a), has been modeled and analyzed and is in very good agreement with the experimental results shown in Fig. 4 (b) and (c), representing crushing force, mean crushing force, and energy absorption. This correlation phase indicates that the FE model is credible and can be used for qualitative investigations.



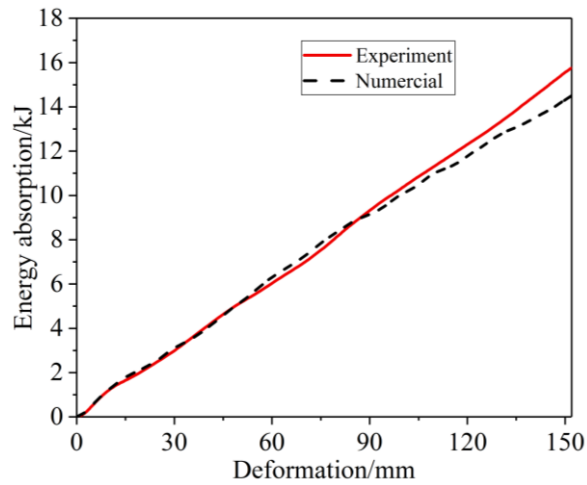
(a)



(b). Crushing force vs. deformation of FTRATS ($L=0$)



(c). Mean crushing force vs. deformation of FTRATS (L=0)



(d). Energy absorption vs. deformation of FTRATS (L=0)

Fig.4. Experimental [39] and numerical results

4 Numerical results and discussion

4.1 Effects of cross-sectional configurations

Fig. 5 illustrates the deformation mode of various FTRATSs subjected to axial compression. The fold locations for all specimens occurred at the top and at the bottom of the FTRATSs. In addition, it can also be seen from Fig. 5 that five-cell (A5) and seven-cell (A7) FTRATSs present a progressive collapse, while the other specimens exhibit Euler deformation in some of the cases. Besides, foam-filled structures are more prone to progressive ductile-plastic collapse deformation due to the support of the foam core and the interaction between the foam and the tube wall [37, 46]. As a result, the numerical results demonstrate that the simple incorporation of the aluminum foam filler into the twelve hollow right angles thin-walled tubes presents a more stable folding mode than the hollow tubes. In addition, in the case of the same number of foam fillers,

more cells in the tube refer to more tube walls in contact with the aluminum foam, resulting in a more stable deformation mode for FTRATS. For example, the deformation of A3-3 is more stable than A1-3. For instance, the deformation of A3-3 is more stable than A1-3.

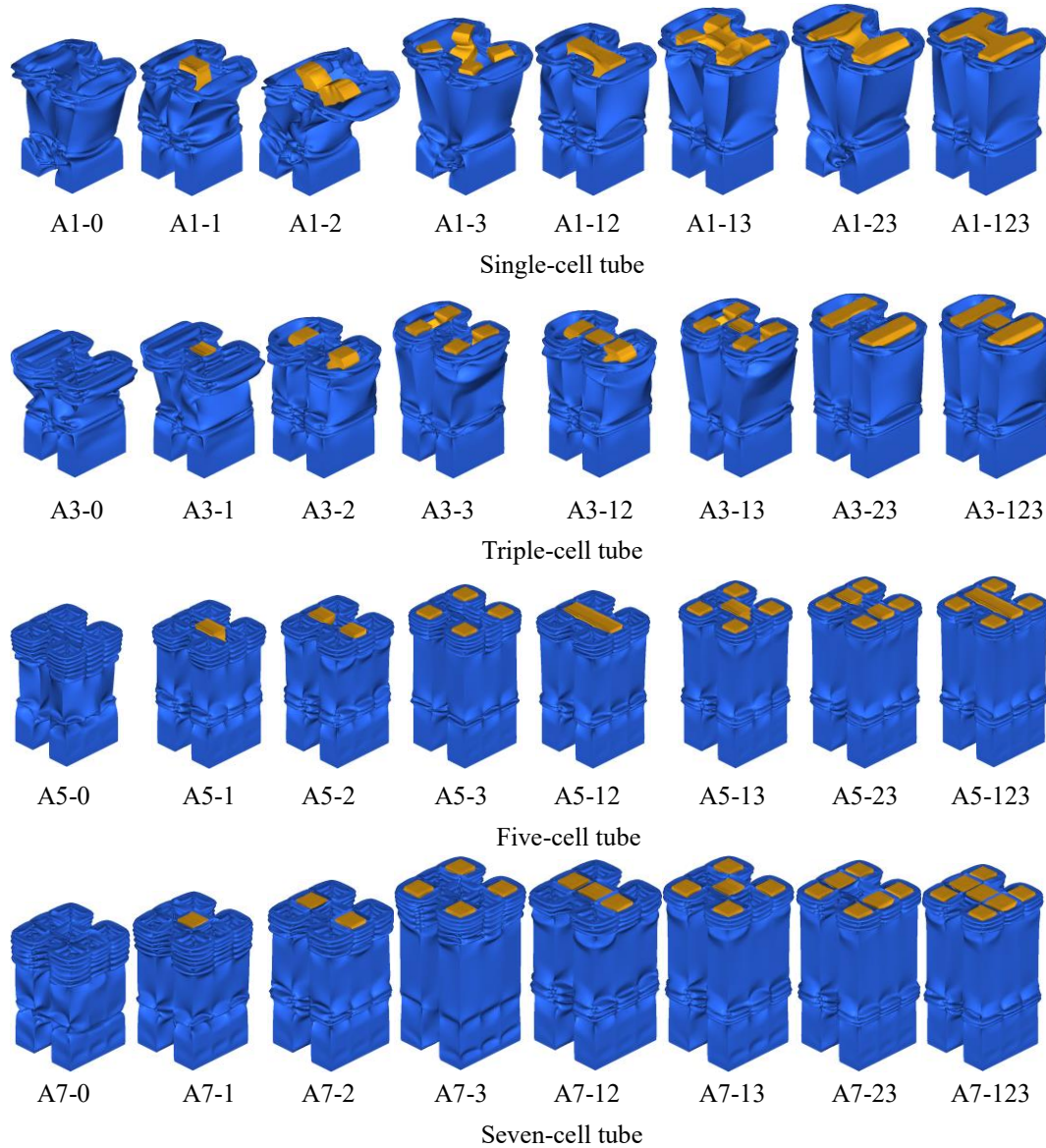
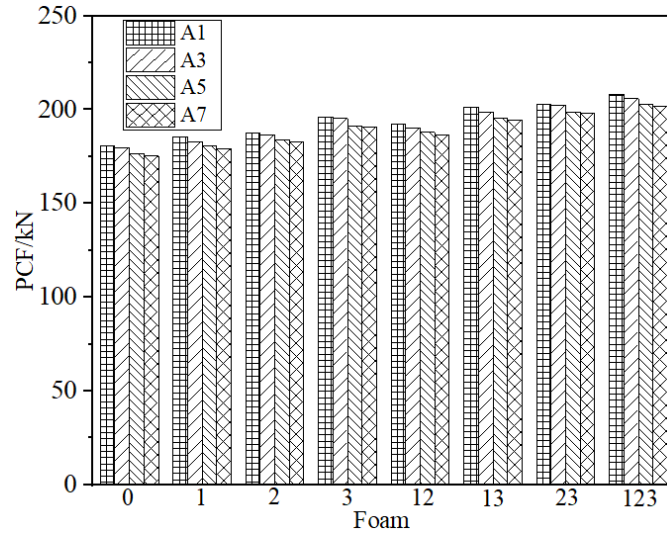


Fig. 5. The topological configurations and deformation mode of FTRATSs.

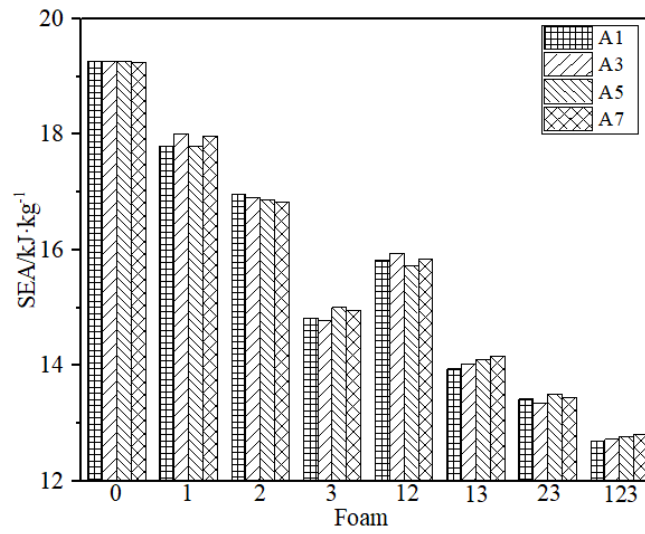
The influence of cross-sectional configurations on the crashworthiness, including PCF, SEA, MCF, Dmax, and CLE, are plotted in Fig.6. Considering PCF in Fig. 6(a), it can be noticed that A1 and A3 are always greatest. Under the same foam filler, the SEA (Fig 6(b)) is almost unchanged.

The MCF in Fig. 6(c) of A5 with foam-0 was the highest. For foam-1, foam-2,

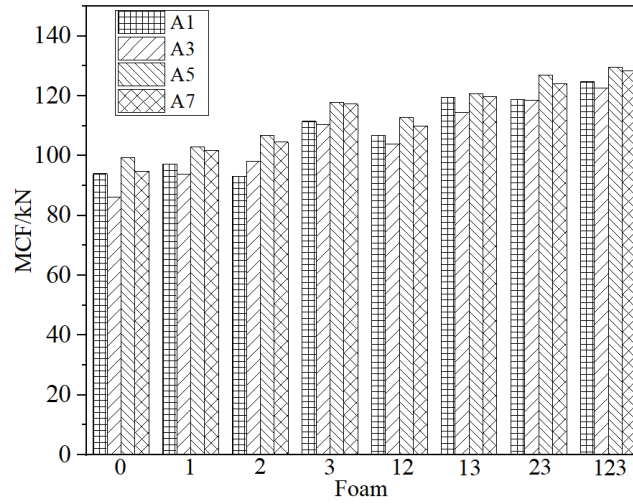
foam-3, foam-12, foam-23, and foam-123, the MCF of A5 and A7 are higher than those of the other two cross-sectional configurations. From Fig.6(d), the D_{max} of A1 and A3 were higher than those of the other two FTRATSs under the same foam distribution. As shown in Fig.6(e), the CLE of A5, followed by A7, is higher than A1 and A3 under the same distribution.



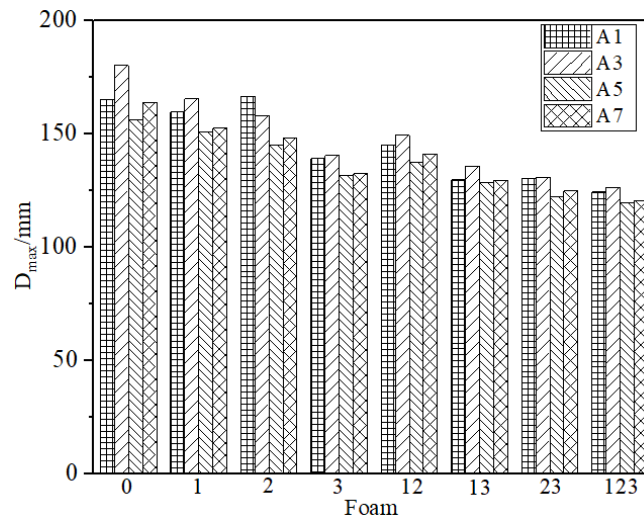
(a) PCF



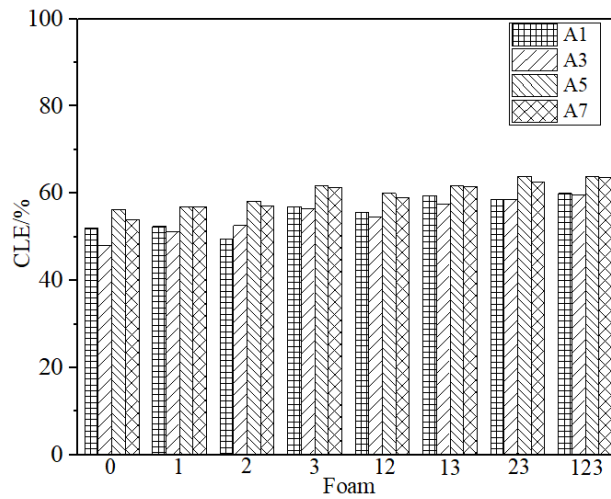
(b) EA



(c) MCF



(d) D_{max}



(e) CLE

Fig.6. The effects of a different distribution of FTRATS

4.2 Effects of foam filler distribution

The friction between the foam core and the inner surface of the tube is the primary

interaction mechanism that significantly affect the crashworthiness performance [60-62]. Consequently, a more stable deformation mode can be achieved at greater friction between the tube wall and the aluminum foam provided by more aluminum foam filled into the thin-walled tube. For example, the deformation of A1-3 is closer to a stable and progressive collapse than A1-1.

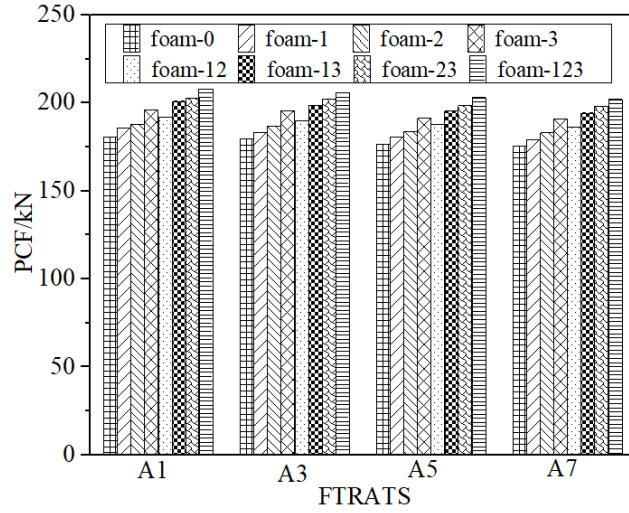
Fig.7 compares the crashworthiness indicators of PCF, SEA, MCF, Dmax, and CLE, which are used to investigate foam filler distribution effects. The PCF of these FTRATSs are shown in Fig. 7 (a), from which it can be noticed that the foam filler distribution is sensitive to PCF with the same cross-section configuration patterns. Besides, foam-123 had the highest PCF value in the four cross-sectional configurations. The structure with full-foam filling is the best when only focusing on the PCF performance.

Fig. 7(b) provides the SEA of all four cross-section configuration patterns. The SEA of foam-0, foam-1, foam-2, foam-12, foam-23 and foam-123 decreased sequentially with the same cross-section configuration. In addition, foam-123 had the lowest SEA since foam-123 generated the highest PCF and the lowest deformation.

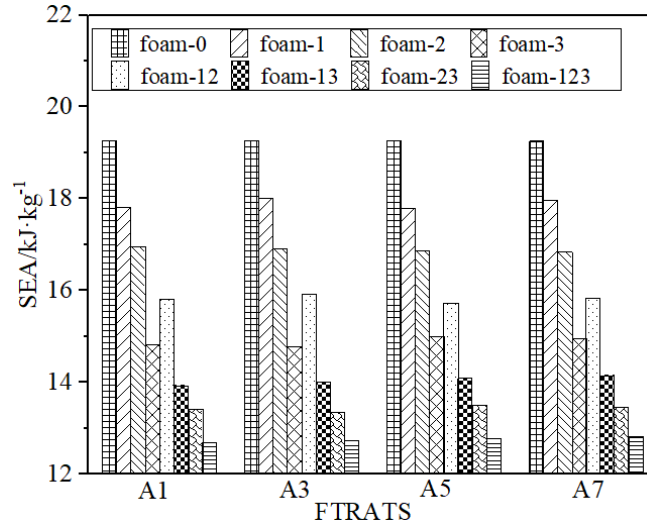
From Fig. 7(c), the MCF values of foam-13, foam-23, foam-123, and foam-3 were greater than those of the other four cross-section configuration patterns, which is similar to the PCF trend. Fig. 7(d) demonstrates that the deformation could be divided into two grades:

- Foam-0, foam-1, foam-2, and foam-12 were the higher grade, whose Dmax values fluctuated between 128 (mm) and 181 (mm).
- Foam-3, foam-13, foam-23, and foam-123 were in the lower grade, and their Dmax values increased from 119 (mm) to 128 (mm).

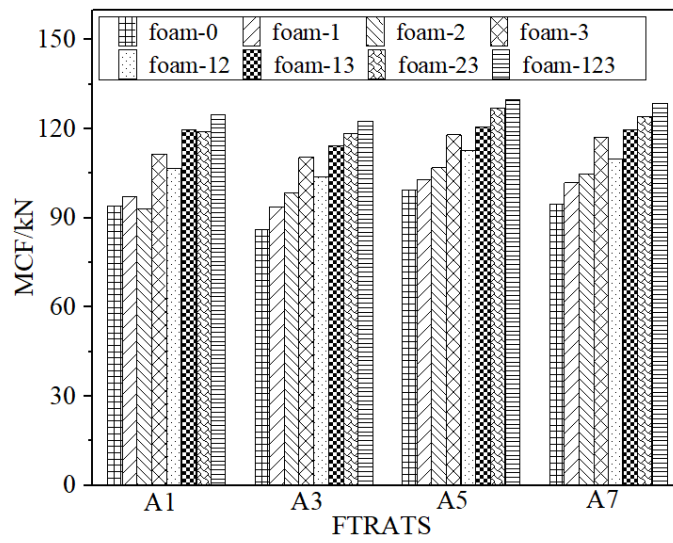
A proper foam filler pattern could significantly improve the CLE of the FTRATSs. For example, foam-3, foam-13, foam-23, and foam-123 were notably higher than the other foam filler distributions. Moreover, foam-123 had the highest CLE in all the other cross-section configuration patterns, except for the A5 cross-section configuration, as shown in Fig. 7(e). For A5, the CLE of foam-23 was slightly higher than foam-123.



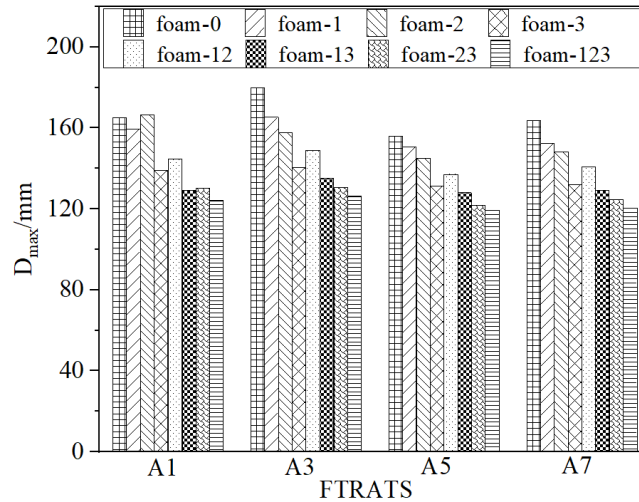
(a) PCF



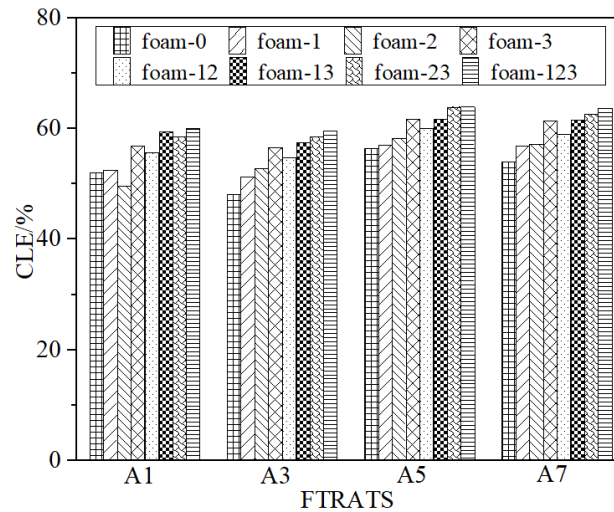
(b) SEA



(c) MCF



(d) D_{max}



(e) CLE

Fig.7. The effects of the different distribution of FTRATS

The above analysis suggests that both the cross-section configuration and the distribution of foam filler influence the crushing behaviors of the FTRATSs, while the degree of the effect differs for these two factors. The cross-section configuration and the distribution of foam filler influence each other. It is, therefore, problematic to determine any relationships between cross-section configuration and foam filler distribution due to the lack of definite trends. The complex proportional assessment (COPRAS) method, a multi-criteria decision-making tool, is then employed to rank the performance of FTRATSs under axial impact [63-65] to extract the best candidate.

4.3 Select the best FTRATS according to the COPRAS method

4.3.1 COPRAS method

The COPRAS method is used to select the optimal solution considering both ideal and least preferred solutions by considering the alternatives' performance with different criteria and the corresponding criteria weights [63-65]. The steps of using the COPRAS method to evaluate are divided into the following six steps [63-65]:

- Step 1: Define the initial decision matrix X.

$$X = [x_{ij}]_{mn} = \begin{bmatrix} x_{11} & x_{12} & \cdots & x_{1n} \\ x_{21} & x_{22} & \cdots & x_{2n} \\ \cdots & \cdots & \cdots & \cdots \\ x_{m1} & x_{m2} & \cdots & x_{mn} \end{bmatrix} \quad (10)$$

where x_{ij} is the performance value of the i -th alternative on the j -th criteria, m is the number of design alternatives, while n is the number of criteria.

- Step 2: Determine the nondimensionalized matrix R.

A nondimensionalized matrix R , which is used for dimensionless processing, is proposed to convert the entire matrix X .

$$R = [r_{ij}]_{mn} = \frac{x_{ij}}{\sum_{i=1}^m x_{ij}} \quad (11)$$

where the entry x_{ij} is the absolute value for each criterion, $\sum x_{ij}$ represents the summation for several positive decisions.

- Step 3: Fix the weighted normalized decision matrix D.

$$D = [y_{ij}] = r_{ij} \times w_j \quad (12)$$

where the r_{ij} represents the normalized performance value of the i -th alternative on the j -th criterion, and w_j is the j -th criterion's weight. $\sum_{k=1}^j w_j = 1$.

- Step 4: Define the weighted w_j .

The w_j could be defined as:

$$w_j = \frac{W_j}{G} \quad (13)$$

The total score of all criteria could be defined as:

$$G = \sum_{i=1}^n W_j \quad (14)$$

where the total comparison sets (N) are equal to $N = (n(n-1)/2)$, in which n is the number of selection criteria.

The criterion for determining the weight w_j of j -th is described as:

$$W_j = \sum_{i=1}^m N_{ij} \quad (15)$$

- Step 5: Sum the weighted of beneficial and non-beneficial attributes.

$$S_+ = \sum_{i=1}^m S_{+i} = \sum_{i=1}^m \sum_{j=1}^n y_{+ij} \quad (16)$$

$$S_- = \sum_{i=1}^m S_{-i} = \sum_{i=1}^m \sum_{j=1}^n y_{-ij} \quad (17)$$

$$S_{-min} = \min S_{-i} \quad (18)$$

where the y_{+ij} and y_{-ij} represent the beneficial and non-beneficial attributes, respectively. S_{-min} is the minimal value of S_{-i} . The greater S_{+i} together with the lower S_{-i} , the better is the design concept.

- Step 6: Relative significance or priority Q_i .

$$Q_i = S_{+i} + \frac{S_{-min} \sum_{i=1}^m S_{-i}}{S_{-i} \sum_{i=1}^m (S_{-min}/S_{-i})} \quad (19)$$

A higher value of Q_i indicates a better design case.

- Step 7: Calculate the quantitative utility U_i for the i-th alternative.

$$U_i = \frac{Q_i}{Q_{max}} \times 100\% \quad (20)$$

Where the Q_{max} is the maximum value of the relative significance or priority. A design case with a higher value of U_i is considered desirable.

4.3.2 Selection of the best FTRATS.

The COPRAS method mentioned above was adopted as the multi-criteria decision-making process for its simplicity in selecting the optimal profile. The PCF, SEA, MCF, Dmax, and CLE were selected as evaluation indicators. In addition, PCF, Dmax, and CLE were given the higher weighting factors, followed by MCF and SEA. The associated weightage for each crashworthiness criterion was employed, as shown in Table 4.

Table 4. Weightage setting for each performance indicator

Selection criteria	Number of comparison sets, $N=5(5-1)/2=10$										W_j	w_j
	1	2	3	4	5	6	7	8	9	10		
PCF	3	3	2	2							10	10/40=0.25
SEA	1				2	1	1				5	5/40=0.125
MCF		1			2			1	1		5	5/40=0.125
Dmax			2			3		3		2	10	10/40=0.25
CLE				2			3		3	2	10	10/40=0.25
											40	1

Eq. (10) was adopted to normalize the decision matrix while the weights were

assigned. The corresponding weighted normalized decision matrix shown in appendix A was then proposed based on the simulation results in Fig. 5. The sums of the weighted normalized for both beneficial attributes and non-beneficial attributes were calculated according to Eq. (16) and (17), in which the non-beneficial attributes were PCF and Dmax, which were preferred to achieve a lower value [52]. Furthermore, the relative significance, or priority Q_i and the quantitative utility U_i , were determined by Eq. (18) (19) and (20), as per appendix B. From appendix B, the A5-23 was the best candidate tube for designing an efficient energy absorber, as it presented the highest crash load efficiency, a superior mean crushing force and the lowest deformation. Hence, FTRATS with five-cell and foam filler distribution foam-23 configurations were chosen for the next phase of the study to investigate the influence of thickness and foam filling with the purpose to enhancement the FTRATS's crashworthiness response.

4.4 Crashworthiness performance optimization for FTRAT

4.4.1 Optimizaiton formulation

As mentioned above, configuration A5-23, selected by the COPRAS, will produce a near-optimal design due to its superior CLE, MCF, and deformation. However, this FTRATS does not exhibit desirable gains because of the excessive PCF and lower SEA during impact. Thus, PCF and SEA were set as objective functions in a multiobjective optimization to make relevant structural improvements to the FTRATS and achieve improved energy absorption properties. Besides, the wall thickness and foam density strongly affect the energy absorption performance of a structure [34,39]. As a result, the thickness and foam densities were chosen as the experimental variables, as shown in Fig.8. According to engineering experience, the thickness range of thin-walled beams used in automobiles is between 0.6 mm and 2.5 mm, and the density range of foamed aluminum is 0.17 g/cm^3 to 0.51 g/cm^3 . At the same time, to facilitate manufacturing, the thickness value is limited to one decimal place, and the density value is limited to two decimal places. Therefore, the multiobjective optimization can be described as:

$$\left\{ \begin{array}{l} \text{minimize } [PCF, MCF] \\ \text{s. t. } \left\{ \begin{array}{l} 0.6\text{mm} \leq x_1, x_2 \leq 2.5\text{mm} \\ 0.17\text{g/cm}^3 \leq x_3, x_4 \leq 0.51 \text{ g/cm}^3 \\ \text{round } (x_1, 1) \\ \text{round } (x_2, 1) \\ \text{round } (x_3, 2) \\ \text{round } (x_4, 2) \end{array} \right. \end{array} \right. \quad (20)$$

where X_1 is the thickness of the outer structure, X_2 is the thickness of the inner structure, X_3 is the density of corner foam, X_4 is the density of the inner foam.

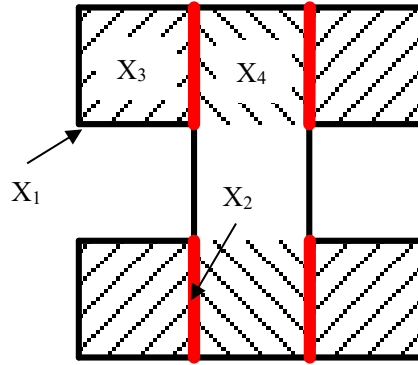


Fig.8. The experimental variables of FTRATS: The thickness of the outer structure (X_1), the thickness of the inner structure (X_2), the density of corner foam (X_3), the density of inner foam (X_4)

4.4.2 Design of experiment

The crashworthiness performance can be evaluated accurately and more efficiently considering a simplified surrogate model, such as a response surface methodology (RSM) or a Kriging model. The design of the experiment technique, Optimal Latin Hypercube (Opt LHD), was adopted to establish this surrogate model. In the RSM model, the minimum number of sample points to construct a response surface model is related to the model order and the number of input variables [66]. Besides, the minimum number of sample points required to construct the model increases as the order increases in the first-order to fourth-order models. The calculation formula for the minimum number of sample points required by the fourth-order response surface model can be defined as [66]. According to our experience, taking 3-4 times the minimum number of experimental groups can provide a good

prediction effect, so 92 sets of experimental we created.

$$N = \frac{(M+1)(M+2)}{2} + 2M \quad (21)$$

Where N is the minimum number of sample points, the M is the number of input variables.

In the kriging model, the formula for calculating the minimum number of samples required to initialize the Kriging approximation model is [66]:

$$N = 2M + 1 \quad (22)$$

Where N is the minimum number of sample points, the M is the number of input variables.

4.5 Optimization results.

4.5.1 Error analysis of metamodels

The design of the experiment and its corresponding objective responses are listed in Appendix B. The accuracy of the RSM and Kriging metamodels' fit to the data is assessed using average error and root mean square (RMS) error, and listed in Table 5. The results indicate that both methods presented a good fit to the result, however, Kriging metamodels were found to predict PCF responses better than the RSM, while the RSM metamodels have an excellent prediction on SEA. Thus, the following optimization design selects the RSM and Kriging metamodels.

Table 5. Accuracies of different metamodels for FTRATs.

	PCF		SEA	
	Average error	RMS error	Average error	RMS error
RSM	0.078	0.096	0.020	0.038
Kriging	0.052	0.076	0.047	0.066
Acceptance level	0.2	0.2	0.2	0.2

4.5.2 Optimization and validation

An adaptive multi-population genetic algorithm (AMGA) method was used to implement the multiobjective optimization for FTRATS. Fig.9 shows the Pareto front observed from the AMGA. Previous research proposed that design engineers may not accept the value of PCF that violates 130 kN [36]. The optimal design of FTRATS with a PCF constrained under 130 kN, corresponding to Pareto fronts masked as a red dot, was obtained and graphed in Fig.9. The detailed optimal design parameters are listed in Table 6.

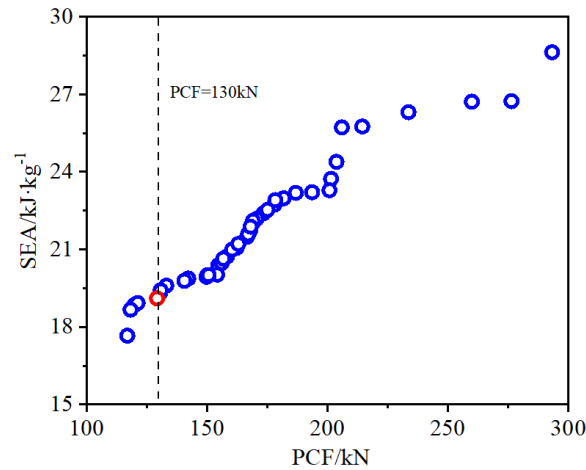


Fig.9. Pareto fronts of FTRATS

Table 6. Optimal design parameters of FTRATS with PCF under 130kN.

X_1 (mm)	X_2 (mm)	X_3 (g/cm ³)	X_4 (g/cm ³)
0.8	2.3	0.37	0.33

The dynamic response and the energy absorption performance of the best FTRATS selected from COPRAS and the optimal FTRATS are shown in Fig.10 and Table 7. It can be seen from Fig.10 that there are no unstable buckling deformation modes which can be observed in the best FTRATS selected from COPRAS followed by the optimisation. Besides, no initial fold appears in the middle of the FTRATS before optimization, while the initial fold occurred at the top, middle and bottom of

the optimal FTRATS.

Further, when deformation reaches the maximum, the best FTRATS obtained by COPRAS appears in undeformed regions located in the middle of the tube. However, for the optimal FTRATS, there are no undeformed regions in the effective deformation area. As a result, the optimal FTRATS with a more reasonable thickness and foam density presented much more progressive deformation modes and thus took better advantage of the energy-absorbing properties of the material than that of the best FTRATS selected from COPRAS. Furthermore, Table 7 demonstrates that the optimal design' PCF does not violate the constraint and has been reduced by 38.83%, while its SEA increased by 38.86%. Therefore, the optimal FTRATS illustrated a superior dynamic response and energy absorption properties than the best FTRATS selected from COPRAS.

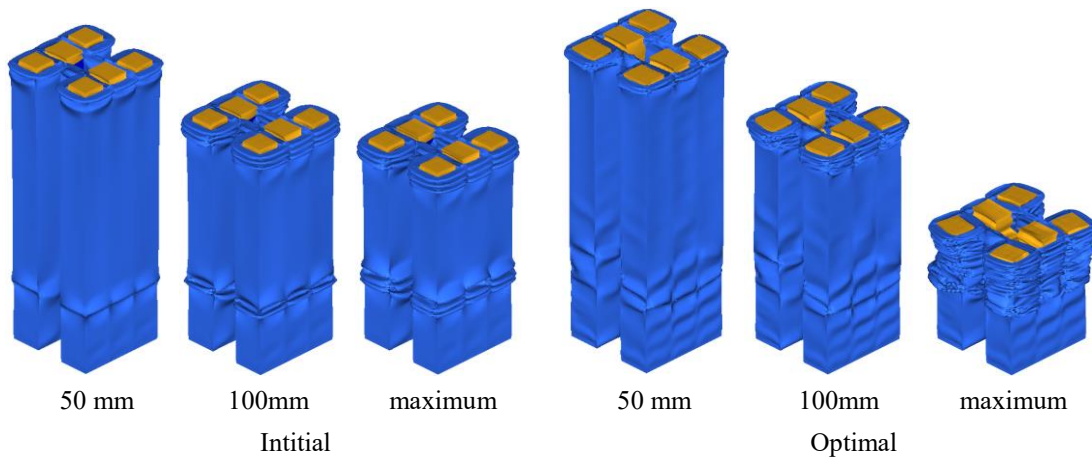


Fig.10. Deformation mode of initial and optimal FTRATSs at different stages

Table 7. Comparison of numerical results of optimal and initial.

PCF(kN)			SEA(kJ/kg)		
Optimal	Initial	Reduction (%)	Optimal	Initial	Reduction (%)
121.53	198.68	38.83	18.76	13.51	38.86

5. Conclusion

The effects of the novel topological configuration of aluminum foam fillers of foam-filled twelve right angles thin-walled structures (FTRATS) on dynamic deformation and crashworthiness response were investigated for the first time, coupling the complex proportional assessment (COPRAS) and optimisation methods. The energy absorption performance of FTRATSs was compared through the COPRAS method. Numerical results demonstrated that the FTRATS of the five-cell tube with foam filler distribution foam-23 (A5-23 topological configuration type) presents a much more progressive and stable deformation mode, resulting in a superior mean crushing force (MCF), crash load efficiency (CLE) and deformation. The energy absorption characteristic of the best FTRATS selected by COPRAS was further enhanced through multiobjective optimization. The peak crushing force (PCF) and specific energy absorption (SEA) of the optimal FTRATS were increased by -38.83 % and 38.86%, respectively, compared to the best FTRATS selected by COPRAS. This new process has shown that coupling COPRAS followed by optimisation was an unbiased and efficient method to study and optimize FTRATS structures.

In the future, the energy absorption mechanics and theoretical analysis of FTRATS with nonlinearly graded shapes will be explored, considering the significance of the nonlinearly graded side length.

Acknowledgments

The support of this work by the 2022 Guangxi University Young and Middle-aged Teachers' Basic Research Ability Improvement Project (Grant No. 2022KY0781) is greatly appreciated. The work was also supported by the Special project of Chongqing Banan District Science and Technology Bureau: "Structural lightweight design

technology of car body front longitudinal beam".

Reference

- [1] Yin H, Xiao Y, Wen G, Qing Q, Deng Y. Multiobjective optimization for foam-filled multi-cell thin-walled structures under lateral impact. *Thin-Walled Structures*. 2015;94:1-12.
- [2] Mahmood HF, Paluszny A. Design of Thin Walled Columns for Crash Energy Management — Their Strength and Mode of Collapse. Society of Automotive Engineers. 1981.
- [3] Wierzbicki T, Abramowicz W. On the crushing mechanics of thin walled structures. *Journal of Applied Mechanics*. 1983;50:727-34.
- [4] Abramowicz W JN. Dynamic progressive buckling of circular and square tubes. *International Journal of Impact Engineering*. 1986;4:243-70.
- [5] Niu X, Xu F, Zou Z. Bionic inspired honeycomb structures and multiobjective optimization for variable graded layers. *Journal of Sandwich Structures and Materials*. 2022.
- [6] Niu X, Xu F, Zou Z, Fang T, Zhang S, Xie Q. In-plane dynamic crashing behavior and energy absorption of novel bionic honeycomb structures. *Composite Structures*. 2022;299:116064.
- [7] Gibson L, Ashby M. Cellular solid: structure and properties (Second Edition): Cambridge University Press, 1997.
- [8] Goyal S, Anand CS, Sharma SK, Sharma RC. Crashworthiness analysis of foam filled star shape polygon of thin-walled structure. *Thin-Walled Structures*. 2019;144.
- [9] Najafi A, Rais-Rohani M. Mechanics of axial plastic collapse in multi-cell, multi-corner crush tubes. *Thin-Walled Structures*. 2011;49:1-12.
- [10] Mamalis AG, Manolacos DE, Baldoukas AK, Viegelaan GL. Energy dissipation and associated failure modes when axially loading polygonal thin-walled cylinders. *Thin-Walled Structures*. 1991;12:17-34.
- [11] Tran T, Hou S, Han X, Tan W, Nguyen N. Theoretical prediction and crashworthiness optimization of multi-cell triangular tubes. *Thin-Walled Structures*. 2014;82:183-95.

- [12] He Q, Ma DW. Parametric study and multiobjective crashworthiness optimisation of reinforced hexagonal honeycomb under dynamic loadings. *International Journal of Crashworthiness*. 2015;20:495-509.
- [13] Qiu N, Gao Y, Fang J, Feng Z, Sun G, Li Q. Crashworthiness analysis and design of multi-cell hexagonal columns under multiple loading cases. *Finite Elements in Analysis and Design*. 2015;104:89-101.
- [14] Qiu N, Gao Y, Fang J, Feng Z, Sun G, Li Q. Theoretical prediction and optimization of multi-cell hexagonal tubes under axial crashing. *Thin-Walled Structures*. 2016;102:111-21.
- [15] Qiu N, Gao Y, Fang J, Sun G, Kim NH. Topological design of multi-cell hexagonal tubes under axial and lateral loading cases using a modified particle swarm algorithm. *Applied Mathematical Modelling*. 2018;53:567-83.
- [16] Chen Y, Bai Z, Zhang L, Wang Y, Sun G, Cao L. Crashworthiness analysis of octagonal multi-cell tube with functionally graded thickness under multiple loading angles. *Thin-Walled Structures*. 2017;110:133-9.
- [17] Zhang L, Bai Z, Bai F. Crashworthiness design for bio-inspired multi-cell tubes with quadrilateral, hexagonal and octagonal sections. *Thin-Walled Structures*. 2018;122:42-51.
- [18] Zhang J, Wu L, Chen G, Zhou H. Bending collapse theory of thin-walled twelve right-angle section beams. *Thin-Walled Structures*. 2014;85:377-87.
- [19] Zhang J, Zhou H, Wu L, Chen G. Bending collapse theory of thin-walled twelve right-angle section beams filled with aluminum foam. *Thin-Walled Structures*. 2015;94:45-55.
- [20] Jones N. *Structural Failure. On the Dynamic Inelastic Failure of Beams*. 1989:133-59.
- [21] Yamashita M, Gotoh M, Sawairi Y. Axial crush of hollow cylindrical structures with various polygonal cross-sections: Numerical simulation and experiment. *Journal of Materials Processing Technology*. 2003;140:59-64.
- [22] Zhang J, Chen G, Wu L, Liu Y. Lightweight method of car's front rail based on the theory of thin-walled beam crashworthiness. *Journal of Jilin University*

(Engineering and Technology Edition). 2013;43:1441-6.

[23] Chen G. Research on the theory of the multi-right angles thin-walled beam and application in autobody crashworthiness design. Jilin University, 2014.

[24] Chen G, Lu S, Zhao Z, Chen C, Lou L. Lightweight design of CFRP thin-walled beam bumper with twelve right-angle section. *Automotive Engineering*. 2019;41:232-8.

[25] He Y, Zhang X, Sun J, Shu X, Li X, Su B, et al. Energy absorption of self-similar inspired multi-cell hexagonal tubes. *Engineering Structures*. 2023;277:115455.

[26] Wu F, Chen Y, Zhao S, Hong Y, Zhang Z, Zheng S. Mechanical properties and energy absorption of composite bio-inspired multi-cell tubes. *Thin-Walled Structures*. 2023;184:110451.

[27] Zhang X, Zhang H. Axial crushing of circular multi-cell columns. *International Journal of Impact Engineering*. 2014;65:110-25.

[28] Fang J, Gao Y, Sun G, Qiu N, Li Q. On design of multi-cell tubes under axial and oblique impact loads. *Thin-Walled Structures*. 2015;95:115-26.

[29] Zhang X, Zhang H, Yang C, Leng K. Static and dynamic axial crushing of self-locking multi-cell tubes. *International Journal of Impact Engineering*. 2019;127:17-30.

[30] Li Z, Rakheja S, Shangguan W-B. Crushing behavior and crashworthiness optimization of multi-cell square tubes under multiple loading angles. *Proceedings of the Institution of Mechanical Engineers, Part D: Journal of Automobile Engineering*. 2019;234:1497-511.

[31] Kim H-S. New extruded multi-cell aluminum profile for maximum crash energy absorption and weight efficiency. *Thin-Walled Structures*. 2002:311-27.

[32] Tran T. Study on the crashworthiness of windowed multi-cell square tubes under axial and oblique impact. *Thin-Walled Structures*. 2020;155:106907.

[33] Albak Eİ. Crashworthiness design for multi-cell circumferentially corrugated thin-walled tubes with sub-sections under multiple loading conditions. *Thin-Walled Structures*. 2021;164:107886.

[34] Ha NS, Pham TM, Chen W, Hao H, Lu G. Crashworthiness analysis of bio-inspired fractal tree-like multi-cell circular tubes under axial crushing. *Thin-Walled Structures*.

2021;169:108315.

[35] Gao Z, Zhang H, Zhao J, Ruan D. The axial crushing performance of bio-inspired hierarchical multi-cell hexagonal tubes. *International Journal of Mechanical Sciences*. 2023;239:107880.

[36] Yin H, Wen G, Liu Z, Qing Q. Crashworthiness optimization design for foam-filled multi-cell thin-walled structures. *Thin-Walled Structures*. 2014;75:8-17.

[37] Gibson L, Ashby M. *Cancellous bone, Cellular solids: Structure & Properties*. New York: Pergamon Press. 1988:316-31.

[38] Hanssen AG, Langseth M, Hopperstad OS. Static crushing of square aluminium extrusions with aluminium foam filler. *International Journal of Mechanical Sciences*. 1999;41:967-93.

[39] Hanssen AG, Langseth M, Hopperstad OS. Static and dynamic crushing of square aluminium extrusions with aluminium foam filler. *International Journal of Impact Engineering*. 2000:347-283.

[40] Chen W, Wierzbicki T. Relative merits of single-cell, multi-cell and foam-filled thin-walled structures in energy absorption. *Thin-Walled Structures*. 2001;39:287-306.

[41] Santosam SP, Wierzbicki T, Hanssen AG, Langseth M. Experimental and numerical studies of foam-filled sections. *International Journal of Impact Engineering*. 2000:509-34.

[42] Deshpande VS, Fleck NA. Isotropic constitutive models for metallic foams. *Journal of the Mechanics and Physics of Solids*. 2000;48:1253-83.

[43] Duarte I, Krstulović-Opara L, Vesenjak M. Characterisation of aluminium alloy tubes filled with aluminium alloy integral-skin foam under axial compressive loads. *Composite Structures*. 2015;121:154-62.

[44] Duarte I, Vesenjak M, Krstulović-Opara L, Ren Z. Static and dynamic axial crush performance of in-situ foam-filled tubes. *Composite Structures*. 2015;124:128-39.

[45] Duarte I, Krstulović-Opara L, Vesenjak M. Axial crush behaviour of the aluminium alloy in-situ foam filled tubes with very low wall thickness. *Composite Structures*. 2018;192:184-92.

[46] Duarte I, Krstulović-Opara L, Dias-de-Oliveira J, Vesenjak M. Axial crush

performance of polymer-aluminium alloy hybrid foam filled tubes. *Thin-Walled Structures*. 2019;138:124-36.

[47] Vesenjak M, Duarte I, Baumeister J, Göhler H, Krstulović-Opara L, Ren Z. Bending performance evaluation of aluminium alloy tubes filled with different cellular metal cores. *Composite Structures*. 2020;234:111748.

[48] Chilla V, Mondal DP, Ram GDJ, Mukherjee M. Processing of in-situ aluminium foam-filled stainless steel tube with foam-tube bonding for enhanced crashworthiness. *Journal of Manufacturing Processes*. 2022;82:488-500.

[49] Zhao M, Wu X, Du J, Yuan H, Wang X, Shi Z, et al. Plastic behavior of the foam-filled sandwich beam with circular tube core under transverse loading. *Engineering Structures*. 2022;268.

[50] Zarei HR, Kröger M. Crashworthiness optimization of empty and filled aluminum crash boxes. *International Journal of Crashworthiness*. 2007;12:255-64.

[51] Zhang T, Liu Z, Li S, Lei J, Wang Z. Dynamic response and energy absorption performance of aluminum foam-filled sandwich circular tubes under internal blast loading. *International Journal of Impact Engineering*. 2023;173:104458.

[52] Sun G, Liu T, Huang X, Zheng G, Li Q. Topological configuration analysis and design for foam filled multi-cell tubes. *Engineering Structures*. 2018;155:235-50.

[53] RAGLAND CL, FESSAHAIE O, ELLIOTT D. Evaluation of frontal offset/oblique crash test conditions. *PROCEEDINGS OF 17TH INTERNATIONAL TECHNICAL CONFERENCE ON THE ENHANCED SAFETY OF VEHICLES CD ROM*. Amsterdam , Netherlands2001.

[54] Bigdeli A, Nouri MD. A crushing analysis and multiobjective optimization of thin-walled five-cell structures. *Thin-Walled Structures*. 2019;137:1-18.

[55] Li Z, Chen R, Lu F. Comparative analysis of crashworthiness of empty and foam-filled thin-walled tubes. *Thin-Walled Structures*. 2018;124:343-9.

[56] Pirmohammad S, Marzdashti SE. Crushing behavior of new designed multi-cell members subjected to axial and oblique quasi-static loads. *Thin-Walled Structures*. 2016;108:291-304.

[57] Xu F, Zhang S, Wu K. Study on crashworthiness design criteria and method of

tubular structures with power exponent distribution of thickness. *Explosion and shock waves*. 2019;39:035103-1--9.

[58] Langseth, M., Hopperstad OS. Static and dynamic axial crushing of square thin-walled aluminum extrusions. *International Journal of Impact Engineering*. 1996;18:949-68.

[59] G HA, S HO, M. L. Crushing of square aluminium extrusions with aluminium foam filler - numerical analyses. *Transactions on the Built Environment*. 1998;32.

[60] Duarte I, Vesenjajk M, Krstulović-Opara L, Ren Z. Compressive performance evaluation of APM (Advanced Pore Morphology) foam filled tubes. *Composite Structures*. 2015;134:409-20.

[61] Duarte I, Vesenjajk M, Krstulović-Opara L. Compressive behaviour of unconstrained and constrained integral-skin closed-cell aluminium foam. *Composite Structures*. 2016;154:231-8.

[62] Duarte I, Vesenjajk M, Krstulović-Opara L, Ren Z. Crush performance of multifunctional hybrid foams based on an aluminium alloy open-cell foam skeleton. *Polymer Testing*. 2018;67:246-56.

[63] Chatterjee P, Chakraborty S. Material selection using preferential ranking methods. *Materials & Design*. 2012;35:384-93.

[64] Chatterjee P, Athawale VM, Chakraborty S. Materials selection using complex proportional assessment and evaluation of mixed data methods. *Materials & Design*. 2011;32:851-60.

[65] Zavadskas EK, Turskis Z, Tamošaitiene J, Marina V. Multicriteria selection of project managers by applying grey criteria. *Ukio Technologinis ir Ekonominis Vystymas*. 2008;14:462-77.

[66] Lai Y, Jiang X, Fang L, Li M, Li G. Theory and example of isight parameter optimization. *Beihang university*, 2012.

Appendix A: Weighted normalized decision matrix

Terms	Weightages					S ₊	S ₋	Qi	U	Rank
	0.25	0.125	0.125	0.25	0.25					
	Performance indicators									
	PCF(kN)	SEA(kJ/kg)	MCF(kN)	Dmax(mm)	CLE					
A1-0	0.029523	0.03853	0.02661	0.03631	0.02822	0.01520	0.01646	0.03001	0.90929	27
A1-1	0.030292	0.03561	0.02752	0.03509	0.02845	0.01500	0.01635	0.02992	0.90651	28
A1-2	0.030662	0.03392	0.02636	0.03663	0.02692	0.01427	0.01682	0.02876	0.87139	31
A1-3	0.032032	0.02964	0.03157	0.03057	0.03087	0.01537	0.01565	0.03095	0.93768	22
A1-12	0.031389	0.03163	0.03025	0.03191	0.03018	0.01528	0.01583	0.03069	0.92978	24
A1-13	0.032855	0.02787	0.03387	0.02849	0.03228	0.01579	0.01534	0.03168	0.96003	11
A1-23	0.03316	0.02683	0.03367	0.02866	0.03179	0.01551	0.01545	0.03129	0.94793	18
A1-123	0.033974	0.02537	0.03531	0.02731	0.03255	0.01572	0.01532	0.03164	0.95854	13
A3-0	0.02932	0.03852	0.02441	0.03957	0.02607	0.01438	0.01722	0.02854	0.86472	32
A3-1	0.029886	0.03602	0.02656	0.03636	0.02783	0.01478	0.01656	0.02950	0.89388	30
A3-2	0.030474	0.03382	0.02782	0.03471	0.02859	0.01485	0.01630	0.02981	0.90330	29
A3-3	0.031907	0.02955	0.03126	0.03087	0.03068	0.01527	0.01569	0.03081	0.93338	23
A3-12	0.031041	0.03187	0.02941	0.03283	0.02967	0.01508	0.01597	0.03035	0.91948	26
A3-13	0.032473	0.02805	0.03237	0.02980	0.03122	0.01536	0.01557	0.03102	0.93976	21
A3-23	0.033051	0.02669	0.03355	0.02875	0.03179	0.01548	0.01545	0.03125	0.94700	20
A3-123	0.033617	0.02545	0.03471	0.02778	0.03234	0.01561	0.01535	0.03149	0.95409	14
A5-0	0.028808	0.03852	0.02815	0.03431	0.03059	0.01598	0.01578	0.03143	0.95237	15
A5-1	0.029524	0.03559	0.02914	0.03314	0.03091	0.01582	0.01567	0.03138	0.95081	16
A5-2	0.030018	0.03374	0.03027	0.03190	0.03157	0.01589	0.01548	0.03164	0.95882	12
A5-3	0.031211	0.03001	0.03338	0.02891	0.03349	0.01630	0.01503	0.03252	0.98521	5
A5-12	0.030707	0.03146	0.03195	0.03021	0.03258	0.01607	0.01523	0.03208	0.97207	9
A5-13	0.031956	0.02820	0.03420	0.02821	0.03352	0.01618	0.01504	0.03239	0.98138	7
A5-23	0.032446	0.02701	0.03596	0.02682	0.03471	0.01655	0.01482	0.03300	1.00000	1
A5-123	0.033146	0.02554	0.03671	0.02627	0.03469	0.01645	0.01485	0.03287	0.99583	2
A7-0	0.028652	0.03851	0.02682	0.03601	0.02931	0.01549	0.01616	0.03058	0.92645	25
A7-1	0.029239	0.03593	0.02882	0.03350	0.03087	0.01581	0.01568	0.03136	0.95007	17
A7-2	0.029869	0.03367	0.02962	0.03259	0.03105	0.01567	0.01562	0.03129	0.94793	19
A7-3	0.031178	0.02992	0.03319	0.02907	0.03334	0.01622	0.01506	0.03241	0.98198	6
A7-12	0.030456	0.03168	0.03113	0.03100	0.03201	0.01585	0.01537	0.03172	0.96109	10
A7-13	0.031766	0.02833	0.03388	0.02848	0.03339	0.01612	0.01506	0.03231	0.97902	8
A7-23	0.032391	0.02689	0.03516	0.02743	0.03399	0.01625	0.01496	0.03256	0.98640	4
A7-123	0.032977	0.02562	0.02661	0.02651	0.03455	0.01639	0.01487	0.03278	0.99327	3

Appendix B: Design of experiment and simulation results

Terms	Thickness of outter structure(mm)	Thickness of inner structure(mm)	Density of corner foam(g/cm ³)	Density of inner foam(g/cm ³)	PCF(kN)	MCF(kN)
1	1.268	1.373	0.1775	0.4614	133.030	19.028
2	2.145	1.644	0.4577	0.4465	227.955	11.940
3	0.809	2.229	0.4726	0.454	144.200	16.476
4	1.686	1.915	0.3942	0.368	185.909	14.036
5	0.621	2.208	0.2821	0.4241	183.351	21.141
6	2.187	1.936	0.4988	0.3269	235.219	11.742
7	2.312	1.289	0.241	0.1924	199.473	14.197
8	0.934	1.665	0.4913	0.2597	136.787	17.527
9	1.915	1.247	0.3718	0.3605	187.590	13.970
10	1.310	2.396	0.2522	0.3792	153.935	16.714
11	0.851	1.519	0.4689	0.4913	137.658	16.941
12	1.080	1.122	0.1924	0.3419	290.151	22.014
13	0.955	2.166	0.3157	0.1962	194.093	19.874
14	1.790	1.895	0.4764	0.1999	197.957	13.653
15	1.895	0.955	0.3344	0.4764	185.131	14.139
16	1.289	0.851	0.5025	0.2634	150.430	16.421
17	2.270	2.145	0.2671	0.4652	226.226	12.368
18	2.291	0.788	0.3381	0.2186	197.892	13.822
19	1.748	2.375	0.2298	0.2447	177.733	15.421
20	2.103	1.707	0.1737	0.2671	189.969	14.946
21	2.041	0.976	0.4614	0.4988	214.123	12.504
22	2.166	1.08	0.51	0.383	224.149	12.122
23	1.853	2.416	0.4876	0.4091	222.630	12.200
24	1.101	1.477	0.2709	0.1887	270.085	20.969
25	0.871	0.746	0.2447	0.4427	267.110	22.627
26	1.602	0.725	0.4465	0.3755	167.192	15.024
27	1.164	1.331	0.4016	0.3344	136.808	17.357
28	1.644	0.809	0.383	0.2559	156.821	16.097
29	1.185	1.185	0.3082	0.5063	136.561	17.539
30	0.913	0.642	0.4054	0.3307	163.361	20.208
31	0.892	1.957	0.17	0.383	225.334	21.969
32	0.600	1.748	0.4241	0.3643	196.393	19.990
33	1.519	2.041	0.4502	0.4876	192.478	13.577
34	1.393	2.187	0.4838	0.297	179.529	14.464
35	2.354	0.934	0.2373	0.439	208.076	13.347
36	0.684	1.581	0.3643	0.241	211.271	22.082
37	1.456	1.79	0.368	0.2485	158.231	16.079
38	0.704	1.101	0.3755	0.4353	177.287	20.616
39	0.997	0.871	0.3456	0.2111	240.987	21.450
40	0.746	2.354	0.2485	0.2933	195.616	21.719
41	1.018	1.853	0.3605	0.4689	138.704	17.157
42	2.500	1.393	0.4315	0.312	237.914	11.677
43	2.062	0.704	0.2148	0.2522	170.495	15.991

44	1.560	1.185	0.1812	0.226	167.614	19.064
45	1.623	0.767	0.2186	0.4577	151.078	17.034
46	1.790	1.164	0.1962	0.3568	162.245	16.465
47	1.122	1.978	0.2335	0.4951	138.577	17.939
48	2.249	0.663	0.439	0.3045	208.372	12.948
49	2.375	1.226	0.2746	0.3157	209.776	13.230
50	1.059	2.082	0.1887	0.2074	215.071	21.510
51	1.498	1.268	0.2933	0.2896	145.697	17.216
52	1.373	0.600	0.2597	0.2709	221.876	19.869
53	2.396	2.103	0.2746	0.2335	223.384	12.725
54	2.02	0.621	0.3008	0.3531	177.307	14.837
55	2.229	2.27	0.3942	0.4726	238.115	11.598
56	1.247	1.727	0.5063	0.3942	170.307	14.864
57	1.226	0.684	0.4129	0.4838	142.072	16.703
58	2.437	2.062	0.3792	0.3493	240.086	11.603
59	1.999	2.458	0.4278	0.2746	218.050	12.558
60	1.185	2.437	0.383	0.3942	159.146	15.700
61	1.665	1.018	0.297	0.17	149.613	17.324
62	2.458	2.02	0.4166	0.2148	240.107	11.753
63	1.769	1.769	0.2559	0.1812	168.369	16.125
64	1.331	1.31	0.4353	0.1849	147.777	16.951
65	1.727	1.999	0.1849	0.4278	176.160	15.486
66	1.414	2.479	0.3419	0.2746	165.669	15.609
67	0.642	1.038	0.454	0.2373	167.573	21.714
68*	0.663	1.602	0.226	0.2821	349.620	25.372
69	0.767	1.456	0.2634	0.4203	219.535	21.846
70	1.038	1.853	0.3195	0.3381	127.994	18.574
71	2.479	0.892	0.3904	0.4166	228.832	11.994
72	1.143	2.124	0.4427	0.1737	149.946	16.888
73	1.352	0.83	0.3232	0.3904	135.464	17.632
74	2.333	1.623	0.1999	0.4016	213.474	13.271
75	1.707	1.414	0.4801	0.3008	187.749	13.947
76	1.581	2.312	0.312	0.4801	183.863	14.322
77	1.435	1.79	0.2074	0.3082	144.950	17.895
78	0.725	1.059	0.3045	0.3195	295.750	23.451
79	2.124	1.143	0.4652	0.2036	207.153	13.167
80	1.54	1.56	0.2858	0.4129	160.156	15.928
81	0.788	2.291	0.4091	0.2858	123.891	18.575
82	1.978	1.832	0.2896	0.3232	192.336	14.038
83	1.957	2.5	0.3269	0.3718	104.109	6.523
84	1.853	1.686	0.3493	0.51	198.819	13.380
85	2.416	1.54	0.3307	0.4315	229.448	12.057
86	0.976	0.997	0.4951	0.4054	136.628	17.131
87	1.477	1.352	0.4203	0.4502	170.039	14.819
88	2.082	1.498	0.3568	0.2298	196.888	13.772
89	1.936	1.435	0.2223	0.5025	189.468	14.395

90	2.208	2.333	0.2036	0.3456	213.705	13.292
91*	0.83	0.913	0.2111	0.2223	399.084	26.749
92	1.832	2.249	0.3531	0.1775	190.227	14.313

*The FTRATS in terms of 68 and 91 do not reach the maximum deformation when the impactors hit the clamping device, thus the height of the clamping device was reduced from 50 mm to 20 mm to obtain the PCF and MCF of the two FTRATS during the impact.